Insights into defect-mediated nucleation of equilibrium B2 phase in face-centered cubic high-entropy alloys

Abhishek Sharma, Bharat Gwalani, Sriswaroop Dasari, Deep Choudhuri, Yao-Jen Chang, Stéphane Gorsse, An-Chou Yeh, Rajarshi Banerjee

Insights into Defect Mediated Nucleation of the Equilibrium B2 Phase in Face-Centered Cubic High Entropy Alloys

Abhishek Sharma[1]*, Bharat Gwalani[1@], Sriswaroop Dasari[1], Deep Choudhuri[1#], Yao-Jen Chang[2,3], Stephane Gorsse[4], An-Chou Yeh[2,3], and Rajarshi Banerjee[1]*

[1] Department of Materials Science and Engineering, University of North Texas, Denton, TX, 76191, USA

[2] Department of Materials Science and Engineering, National Tsing Hua University, 101, Sec. 2, Kuang-Fu Road, Hsinchu, 30013, Taiwan

[3] High Entropy Materials Center, National Tsing Hua University, 101, Sec. 2, Kuang-Fu Road, Hsinchu, 30013, Taiwan

[4] CNRS, Univ. Bordeaux, Bordeaux INP, ICMCB, UMR 5026, F-33600, Pessac, France

@Presently at Physical and Computational Sciences Directorate, Pacific Northwest National Laboratory, 902 Battelle Blvd, Richland, WA, 99352, USA

#Presently at New Mexico Institute of Mining and Technology, 801 Leroy PI, Socorro, NM, 87801, USA

* Corresponding authors: Abhishek.Sharma@unt.edu, Raj.Banerjee@unt.edu

Abstract:

Though a fine scale second phase distribution is a potent strengthening mechanism for alloys, achieving a high precipitate density is often difficult owing to sluggish precipitation kinetics and limited nucleation sites. More specifically in case of transition element based complex concentrated alloys (CCAs) or High Entropy Alloys (HEAs), precipitation of the equilibrium strengthening phase, such as the ordered B2 phase, can be limited due to its high nucleation barrier for homogeneous precipitation within the face-centered cubic (FCC) matrix. This can lead to the competing homogeneous nucleation of a metastable ordered $L1_2$ phase which has a substantially lower nucleation barrier since it is isostructural with the FCC matrix. Using three different CCAs/HEAs as examples, thermo-mechanical processing has been employed to introduce a large number density of homogeneously distributed heterogeneous nucleation sites within the FCC matrix, to manipulate the phase fraction, morphology, and distribution of B2 precipitates. This approach of tailoring microstructure is widely applicable to other multi-component alloys.

Keywords: *Plastic deformation, defect structures, dislocations, B2, High Entropy Alloys, Complex concentrated Alloys, Heterogeneous Microstructures, Metastable, Intermetallic*

Introduction:

Plastic deformation can result in a high density of crystalline defects in the form of boundaries, dislocations, and vacancies. These defects serve as high energy sites for initiating and accelerating phase transformations. Such defect mediated heterogenous nucleation is an essential microstructural design tool in the context of High Entropy Alloys (HEAs) or Complex Concentrated Alloys (CCAs) for tuning their mechanical properties [1–3]. The significance of heterogeneous nucleation is specifically escalated in the case of multicomponent HEAs/CCAs, as most of these alloys are associated with complex phase fields comprising of multiple equilibrium phases [4,5], The nucleation and growth of these phases, is influenced by competing processes such as recovery and recrystallization, typically associated with the aforementioned defect structures. Intentional introduction of defects can serve to increase such nucleation sites but can also impede the motion of mobile interphase boundaries (and hence, the growth of new phase domains). In such a scenario, the thermal activation results in a competition between defect annihilation by precipitation or by recrystallization which may also result in formation of non-equilibrium or metastable phases. Defects such as twins, sub grain boundaries, deformation bands, and dislocation tangles that are introduced during cold deformation/rolling act as potent sites for heterogenous nucleation due to the inherently high energy associated with them. Therefore, annealing after cold deformation can lead to heterogenous microstructures due to inhomogeneous rates of recrystallization and precipitation of equilibrium/non-equilibrium phases. Multiple reports exist highlighting the microstructural modification and mechanical properties of such heterogeneous microstructures created by following this approach [6–8].

HEA/CCAs offer a variety of phase transformation pathways leading to novel microstructures containing intermetallic phases such as $L1_2$, B2, σ, laves and χ phases [9–12]. For example, in case of an FCC based $Al_{0.2}Ti_{0.3}Co_{1.5}CrFeNi_{1.5}$ alloy, it has been observed that precipitation annealing directly after cold rolling resulted in a discontinuously precipitated nano-lamellar/nano-rod type microstructure consisting of $L1_2$ and FCC phases [8]. This is in contrast to the classical γ+γ' type microstructure comprising of spherical $L1_2$ precipitates which results from solutionizing prior to annealing after cold rolling and is a result of homogeneous precipitation of $L1_2$ phase

within the FCC matrix. The microstructure resulting from such defect mediated discontinuous precipitation leads to improved mechanical properties as well. Similarly, in the case of $Al_{0.3}CoFeNi$, solutionizing after cold rolling followed by annealing at 600°C, leads to eutectoid decomposition into (FCC+$L1_2$) and (BCC+B2) lamellae whereas direct annealing at 700°C followed by 600°C after cold rolling, results in ultrafine grained microstructure of FCC grains containing $L1_2$ precipitates, and BCC grains with B2 precipitates [13]. This also results in improved yield strength along with reasonable ductility.

For the case of an FCC based HEA, when the low temperature phase field comprises of FCC+BCC/B2, the classic nucleation of BCC/B2 based phase is difficult, owing to a high barrier to its nucleation in an FCC matrix. The presence of heterogeneous nucleation sites in this scenario, such as defect structures, can provide interesting possibilities for microstructural designing. The present paper demonstrates this by presenting results from three such FCC based HEAs where homogeneous nucleation of a BCC/B2 phase is energetically unfavorable but possible when mediated by high density of defect structures. The rejection of solute from a supersaturated FCC matrix via such heterogenous nucleation is additionally in competition with nucleation of metastable phases with a lower energy barrier. Thus, interesting possibilities in terms of microstructural design exist, based on the degree and extent of prior processing, choice of annealing temperature and the corresponding equilibrium phase field as well as the thermodynamic and kinetic barrier to nucleation of the related metastable phases. Fairly impressive mechanical properties often ensue with such a heterogenous microstructure resulting from defect mediated nucleation. We propose this route as a design template to microstructural modification extendable to a larger class of precipitation strengthened multicomponent HEAs/CCAs with possible gains in mechanical properties.

Materials and Methods:

Alloys with the nominal chemical compositions $Al_{0.3}CoFeNi$ (9.1Al-30.3Co-30.3Fe-30.3Ni at.%), $Al_{0.5}Co_{1.5}CrFeNi_{1.5}$ (9.1Al-27.3Co-18.1Cr-18.2Fe-27.3Ni at.%) and $Al_{0.3}CoCrFeNi$ (7.0Al-23.3Co-23.3Cr-23.2Fe-23.2Ni at.%) were prepared using a conventional vacuum arc melter. The alloys were flipped at least three times to ensure homogenization of the melt. Microstructural characterization was carried out using Scanning Electron Microscopy (FEI Nova-NanoSEM 230^{TM}/ Hitachi SU8010 FE-SEM), fitted with energy dispersive spectroscopy (EDS) and electron

backscattered diffraction (EBSD) detectors. TSL OIM^{TM} software was used to analyze the EBSD data. Transmission Electron Microscopy (FEI Tecnai G2 TF20™ operating at 200 kV/ JEOL JEM-3000F HRTEM operating at 300 kV) was used to obtain crystallographic information from the phases present in the material. For analysis of compositional partitioning, Atom Probe Tomography (APT) was performed using Cameca LEAP 5000XS 3D Atom Probe Microscope operating at a temperature of 30K with pulse energy of 50nJ, pulse rate of 100 kHz, and a detection rate maintained at 0.005-0.01 atoms/pulse in laser mode. The specimens for TEM and APT were prepared using a FEI Nova 200 dual beam focused ion beam (FIB). The heat-treatments of the respective alloys have been described in the individual sections. All the annealing treatments were performed in encapsulated quartz tubes backfilled with argon. The samples for microstructural analysis were machined using Kent wire saw submerged EDM. Thermodynamic predictions were performed using ThermoCalc and the TCHEA4 database.

Results and Discussions:

To study the defect mediated nucleation of B2 phase, we have selected compositions based on the alloy CoFeNi, which is nearly a single phase random solid solution [14,15]. Previous reports have observed that addition of aluminum to this system promotes ordering tendency and hence the formation of intermetallic precipitates [16–23]. Therefore, such aluminum bearing CoFeNi alloys are ideally suited to study the defect mediated nucleation of precipitating equilibrium phases. The pseudo-binary isopleths generated using CALPHAD, for three such systems, namely $Al_xCoFeNi$, $Al_xCo_{1.5}CrFeNi_{1.5}$ and $Al_xCoCrFeNi$, are reproduced in Figure 1(a) which is an overlapping plot of the relevant sections from the three systems. From the plot, it is clear that the FCC+B2 phase field expands with these alloying additions which clearly established the effect of aluminum in promoting the formation of intermetallic phases. Based on such optimization of aluminum addition in these systems, three previously reported alloy compositions having high temperature FCC single phase-field coupled with an intermediate temperature (FCC+B2) phase-field, were selected for this study: $Al_{0.3}CoFeNi$ [6], $Al_{0.5}Co_{1.5}CrFeNi_{1.5}$ [24] and $Al_{0.3}CoCrFeNi$ [25]. The corresponding phase fractions as a function of temperature are provided in Figures 1(b), (c) and (d).

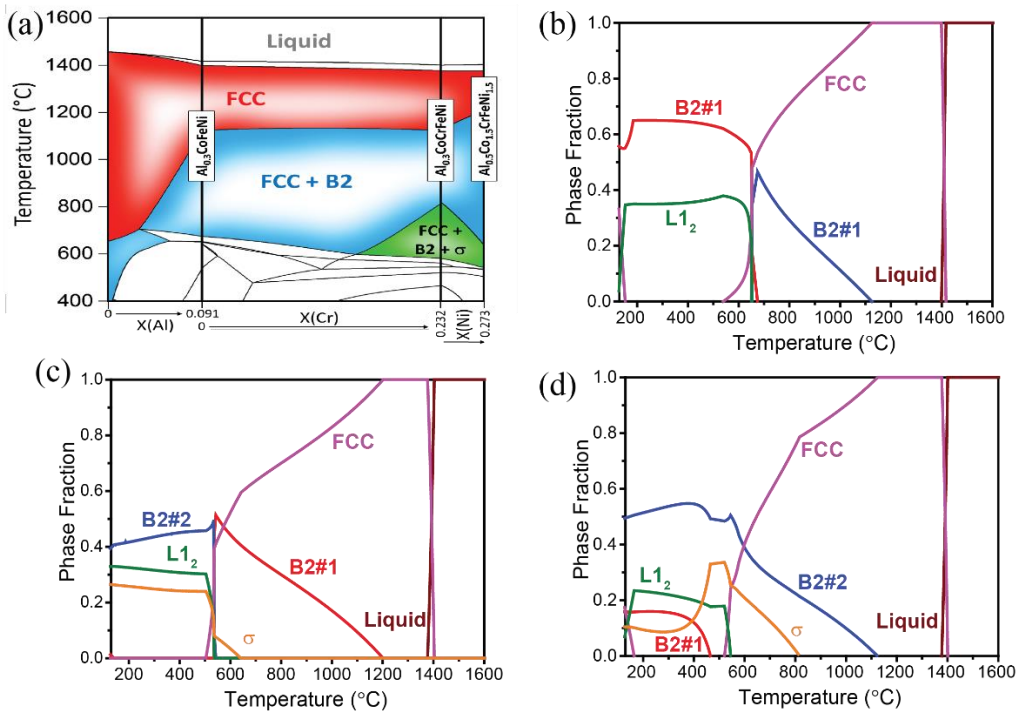

Figure 1: (a) Overlapping pseudo-binary isopleths generated using ThermoCalc, for $Al_xCoFeNi$, $Al_xCo_{1.5}CrFeNi_{1.5}$ and $Al_xCoCrFeNi$ systems. Corresponding phase-fractions as a function of temperature for (b) $Al_{0.3}CoFeNi$. (c) $Al_{0.5}Co_{1.5}FeNi_{1.5}$, and (d) $Al_{0.3}CoCrFeNi$.

To understand the heterogenous nucleation of B2 phase in contrast with its homogenous nucleation, two different processing routes were employed. The first route comprised of homogenizing and cold rolling the cast ingots followed by solutionizing within the respective single-phase FCC phase-fields. These solutionized ingots were then aged within the two-phase FCC+B2 phase fields to promote homogenous nucleation of B2 phase. The second route consisted of cold rolling the homogenized ingot to introduce high density and variety of defects. These defects provide favorable sites for heterogenous nucleation of B2 phase. The cold-rolled samples were then aged within the respective FCC+B2 phase fields. Additionally, depending on the composition, in some cases, metastable phases nucleate homogeneously during either of the processing routes. The resultant microstructures from the two routes are finally compared.

1) Promoting heterogenous nucleation of equilibrium B2 phase in $Al_{0.3}CoFeNi$

Figure 1(a) shows a pseudo-binary isopleth for $Al_xCoFeNi$, with the composition of $Al_{0.3}CoFeNi$ marked by a vertical line. Accordingly, the phase equilibrium at 1250°C is FCC, at 700°C is

(FCC+B2), and at 600°C is (FCC+B2+$L1_2$). The corresponding phase fractions for the respective temperatures are shown in Figure 1(b). The homogenized alloy was cold rolled to ~85% reduction in thickness, and solutionized at 1250°C (CRSA) for 5 mins. As predicted by CALPHAD in Figures 1(a) and (b), the resultant microstructure (in CRSA condition) consists of single-phase FCC grains without any precipitation either within the grains or along the grain boundaries. This is clear from Supplementary Figure 1(a) which is a BSE-contrast SEM image from this condition and from Supplementary Figure 1(b) which is an SADP from this sample showing the [011] zone axis pattern for FCC without any additional superlattice spots.

When this solutionized alloy is further annealed at 700°C (CRSA-700 condition), the microstructure consists of coarse FCC grains with fine B2 grains precipitating along the FCC grain boundaries. This is shown in Figure 2(a) which is a BSE contrast SEM image. Figure 2(b) is a phase map from a triple-junction, generated from EBSD, clearly showing presence of B2 phase along grain boundaries of FCC grains. The $L1_2$ phase is absent which is also supported by the phase stability predicted from CALPHAD (Figures 1(a) and (b)). Although CALPHAD calculations predict a finite onset-driving force for homogeneous nucleation of B2 phase in FCC matrix at 700°C, which is shown in Supplementary Figure S1(c), owing to a higher energy barrier to homogenous nucleation within the FCC matrix, B2 phase, despite being the equilibrium phase at this temperature, is unable to nucleate homogeneously within the grains [6]. Instead, it nucleates along the grain boundaries which serve as heterogenous nucleation sites with a much lower energy barrier to nucleation. The nucleation of B2 phase in this scenario is limited by the volume of grain boundary area available as nucleation sites which in turn depends on the grain size. Therefore, at a larger grain size, the actual volume fraction of B2 phase would be less than the expected equilibrium volume fraction. This suggests towards the possibility of achieving an increase in the B2 phase fraction by reducing the grain size. The second processing route precisely accomplishes this with the added advantage of the grain boundaries in this case being a more potent heterogenous nucleation site, owing to the highly strained microstructure.

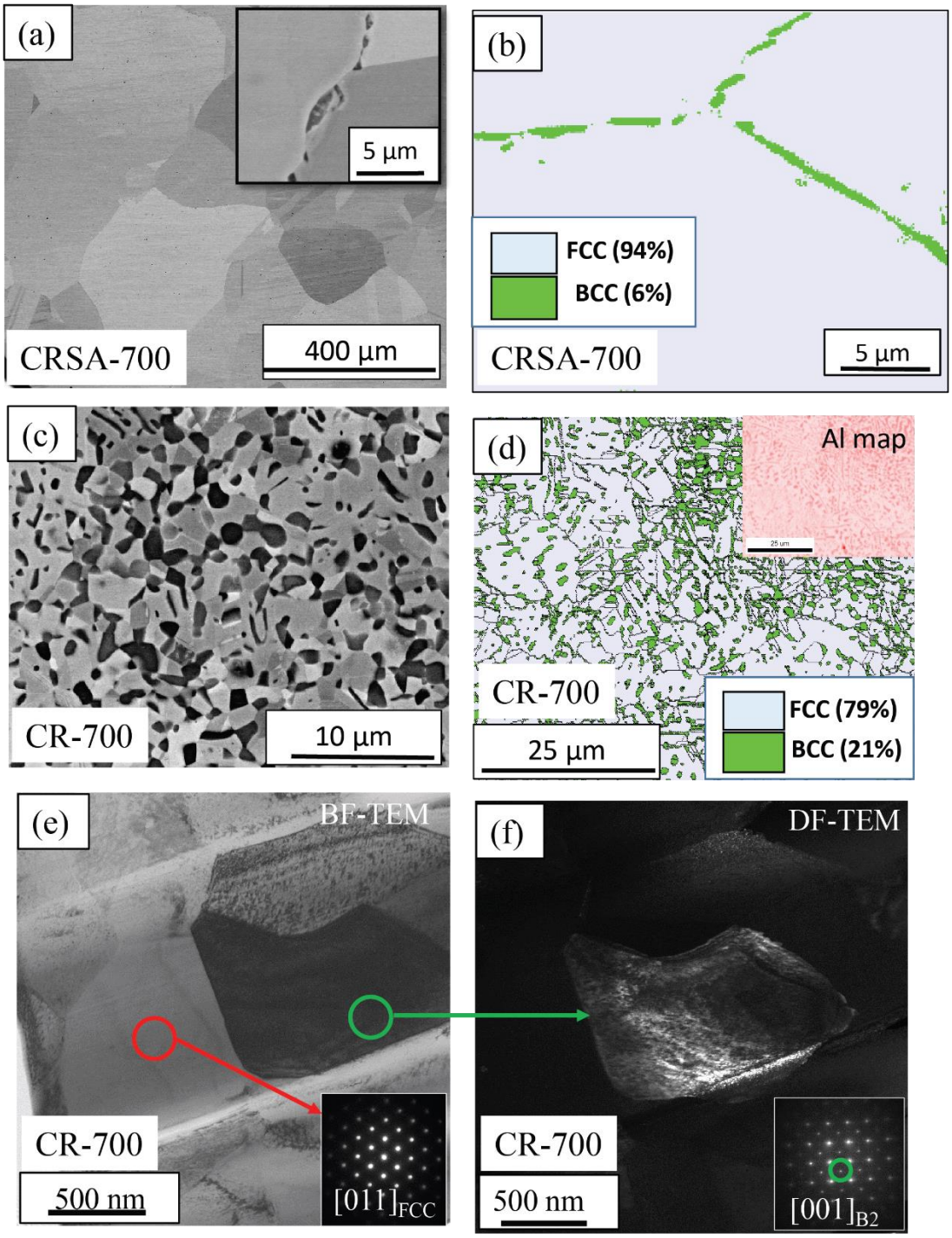

Figure 2: (a) BSE contrast SEM image, and (b) Phase-map from EBSD acquired from a triple junction, both showing microstructure of $Al_{0.3}$CoFeNi in CRSA-700 condition. (c) BSE contrast SEM image, and (d) Phase-map from EBSD, both showing microstructure of $Al_{0.3}$CoFeNi in CR-700 condition. (e) Bright-field TEM image and (f) Dark-field TEM image to confirm the presence of FCC and B2 grains, in CR-700 condition. Figures reprinted from [6]

Hence, when the homogenized and cold-rolled alloy is directly aged at 700°C (CR-700) avoiding the solutionizing step, the result is a fine-grained dual-phase microstructure consisting of FCC and B2 grains. This is depicted in the BSE contrast SEM image in Figure 2(c) along with the phase map from a similar region, shown in Figure 2(d). The crystal structures of the two phases are further confirmed via TEM. Figure 2(e) is a bright-field TEM image showing two adjacent FCC and B2 grains along with the SADP from the FCC grain in the inset. Figure 2(f) is a dark-field TEM image acquired using the B2 superlattice spot along with the corresponding SADP shown in inset, from the B2 grain. Because of a significantly finer FCC grain size and highly strained grain boundaries resulting from the cold-rolling step, a large number of nucleation sites in the form of these grain-boundaries are available for heterogenous nucleation of B2 grains. It appears that the stress concentrations along the grain boundaries such as dislocation pileups and slip steps are such potent heterogenous nucleation sites. The new strain free grains nucleating at such high energy sites eventually grow by consuming the nearby highly deformed grains. Additionally, in parallel to this, new FCC strain free grains may also nucleate and grow at such high energy sites, in process consuming the strained FCC grains, which is the usual mechanism observed during recrystallization. The microstructure is essentially getting recrystallized by both these processes. This has been observed in the case of $Al_{0.3}CoCrFeNi$ as well [7], which will be further discussed in a later section. This results in a fine distribution of both FCC and B2 grains and ultimately precipitation of a higher volume fraction of B2 phase (~21%) than that observed in the case of homogeneous nucleation (~6%).

2) Competing nucleation tendencies of metastable $L1_2$ and the equilibrium B2 phases in $Al_{0.5}Co_{1.5}CrFeNi_{1.5}$

In the previous section, it was demonstrated that homogenous nucleation of equilibrium B2 phase within the FCC matrix, is energetically difficult as compared to its heterogenous nucleation along high energy sites such as strained grain boundaries. Additionally, in some cases, metastable phases may also interfere with this process whenever the barrier to nucleation for such phases is considerably lower than that for the equilibrium phase. Such competition has been captured in the present alloy.

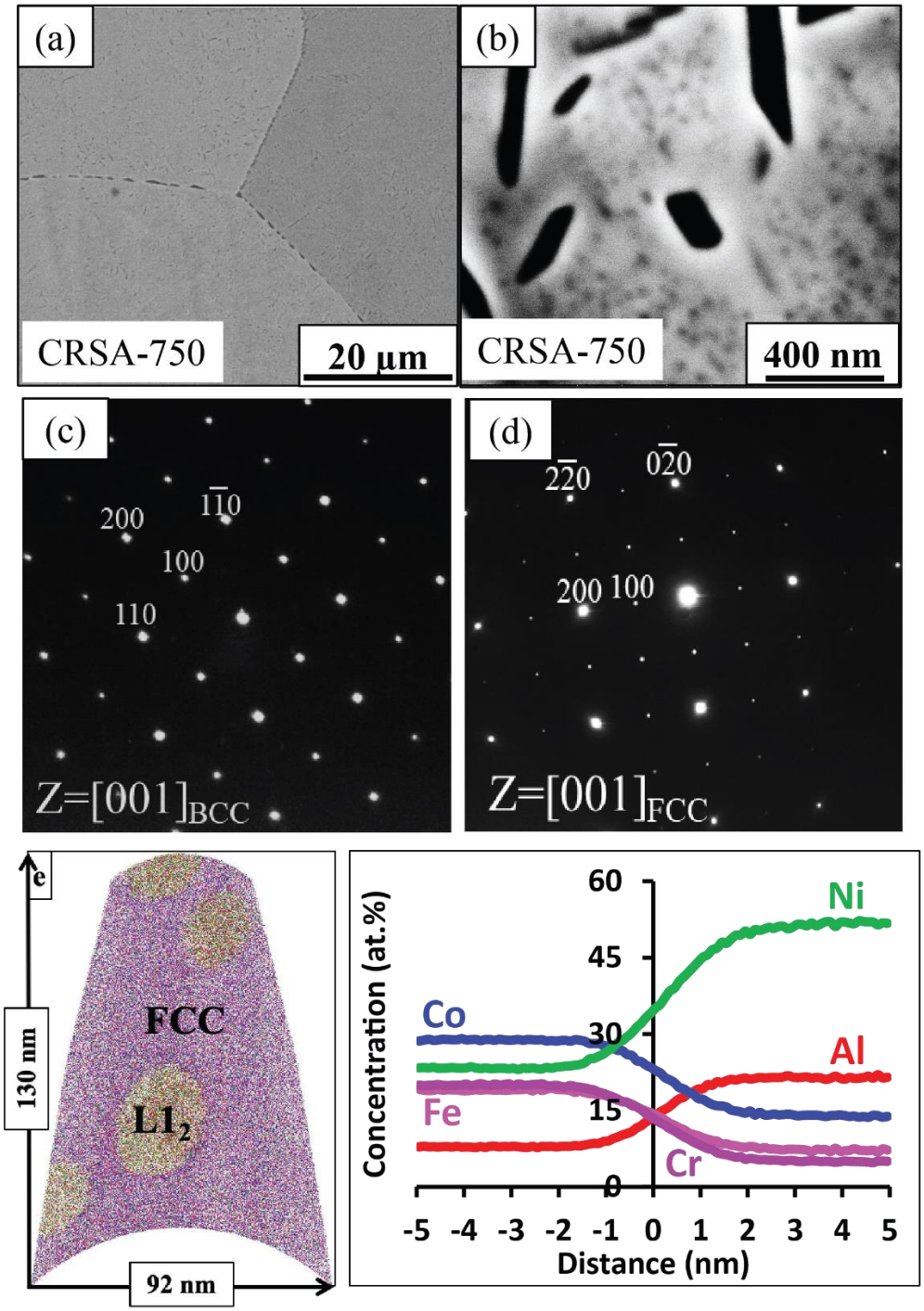

Figure 3: (a) Low magnification, and (b) High magnification BSE contrast SEM image from $Al_{0.5}Co_{1.5}FeNi_{1.5}$ in CRSA-750 condition (c) SADP acquired along [001] zone axis of B2 precipitate. (d) SADP acquired along [001] zone axis of FCC matrix. (e) APT reconstruction from FCC matrix along with a $L1_2$ precipitate. (f) Corresponding proxigram depicting FCC matrix and $L1_2$ precipitate compositions. Figures reprinted from [24] with permission from Elsevier.

The $Al_{0.5}Co_{1.5}CrFeNi_{1.5}$ alloy after homogenizing, and cold rolling to ~60% reduction in thickness, followed by solutionizing at 1250°C for 5 mins, was annealed at 750°C for 50 hrs (CRSA-750 condition). Figure 3(a) is a BSE contrast SEM image showing the microstructure in CRSA-750 condition which consists of coarse recrystallized FCC grains and B2 precipitates along the grain boundaries as well as within the grains near the grain boundaries, as shown in Figure 3(b) which is a higher magnification BSE contrast SEM image from near a grain boundary. Figure 3(c) is a SADP from one such precipitate acquired along the [001] zone axis of the B2 precipitate. This microstructure is similar to that observed for the previous alloy in CRSA-700 condition. However, in the present condition, additionally within the FCC grains, fine scale $L1_2$ precipitates are also present which appear as fine pockets dispersed in FCC matrix between the coarse B2 plates. This is also shown in Figure 3(b). Figure 3(d) is an SADP along [001] zone, captured from within the FCC grains showing superlattice spots confirming presence of $L1_2$ precipitates. Such $L1_2$ precipitates have been captured in APT reconstruction from the FCC grain, as shown in Figure 3(e) along with the corresponding proxigram showing the composition of the $L1_2$ precipitate and the matrix. Based on the composition estimated from APT, it appears that the precipitates may have the stoichiometry corresponding to $(Ni,Fe,Co)_3(Al,Cr)$, assuming an Ni_3Al type stoichiometry [26,27]. For the case of current alloy composition, although $L1_2$ is not an equilibrium phase at this temperature as per CALPHAD calculations [24], it stills forms as a metastable transient phase having a low barrier to its homogenous nucleation within the super-saturated FCC matrix. The B2 phase has a higher onset-driving force for homogenous nucleation within the FCC matrix which is depicted in Figure 4. But despite being an equilibrium phase (based on CALPHAD), B2 is unable to nucleate due to a high barrier to homogenous nucleation in an FCC matrix. Such high barrier to nucleation of B2 is due to the high interfacial energy associated with the FCC/B2 interface as compared to that for $L1_2$/FCC [7,24]. Hence, although $L1_2$ is a meta-stable phase at this temperature, it is able to nucleate homogeneously whereas B2, despite being equilibrium phase, is only able to nucleate heterogeneously along grain boundaries.

To understand which way this competition between a metastable phase and an equilibrium phase is biased by promoting heterogenous nucleation, the alloy was annealed directly at 750°C after cold-rolling step, entirely avoiding the solutionizing step, i.e. CR-750 condition. Figure 5(a) is a BSE contrast SEM image showing the microstructure in CR-750 condition which consists of fine recrystallized pockets distributed within un-recrystallized FCC regions. The recrystallized pockets

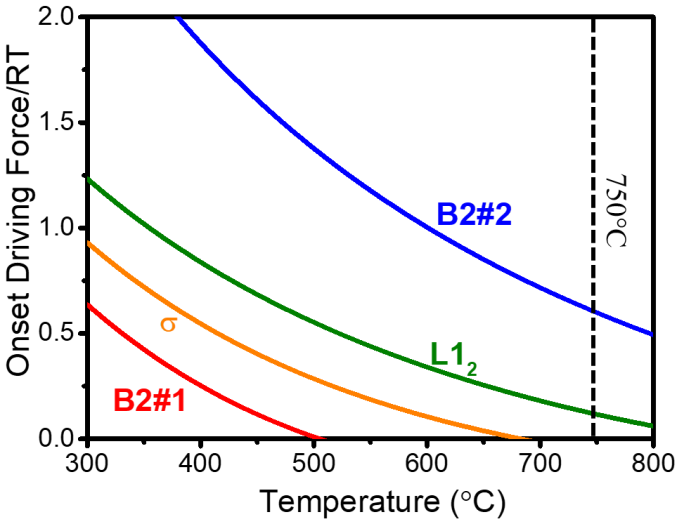

Figure 4: Normalized onset-driving forces for homogeneous nucleation within an FCC matrix for various phases in alloy $Al_{0.5}Co_{1.5}CrFeNi_{1.5}$ determined using ThermoCalc, as a function of temperature. Figure reprinted from [24] with permission from Elsevier.

consist of fine FCC recrystallized grains devoid of $L1_2$ along with fine-scale B2 precipitates both within the grains as well as along grain boundaries resembling the microstructure observed in CR-700 condition in previous section. Examples of these two cases are depicted in Figures 5(c) and (d), both of which are dark-field TEM images. Just like in previous section for the case of $Al_{0.3}CoFeNi$, the strain build-up along grain boundaries due to cold rolling, aid in nucleation of B2 grains along with concurrent recrystallization of the microstructure. Detailed report of this condition observed that some of these intra-granular B2 precipitates follow Nishiyama-Wasserman (N-W) orientation relationship whereas some follow the Kurdjumov-Sachs (K-S) orientation relationship with the parent FCC matrix [24]. Such an occurrence of B2 phase in multiple orientation relationships with the parent FCC lattice has been reported previously in case of $Al_{0.3}CoCrFeNi$ [28]. For the same alloy, it was observed that K-S oriented B2 plates nucleate along broad faces of twins whereas N-W oriented B2 pockets nucleate along regions where two different variants of twins intersect within a single grain. Nucleation along such intersections is aided owing to a high degree of locally altered matrix orientation. Pitsch oriented B2 pockets were also observed to nucleate along some of such intersections.

The mechanism of B2 nucleation in FCC HEAs along twin interfaces has been discussed in detail previously [29] where it was discovered that the FCC to B2 transformation is a mixed-mode

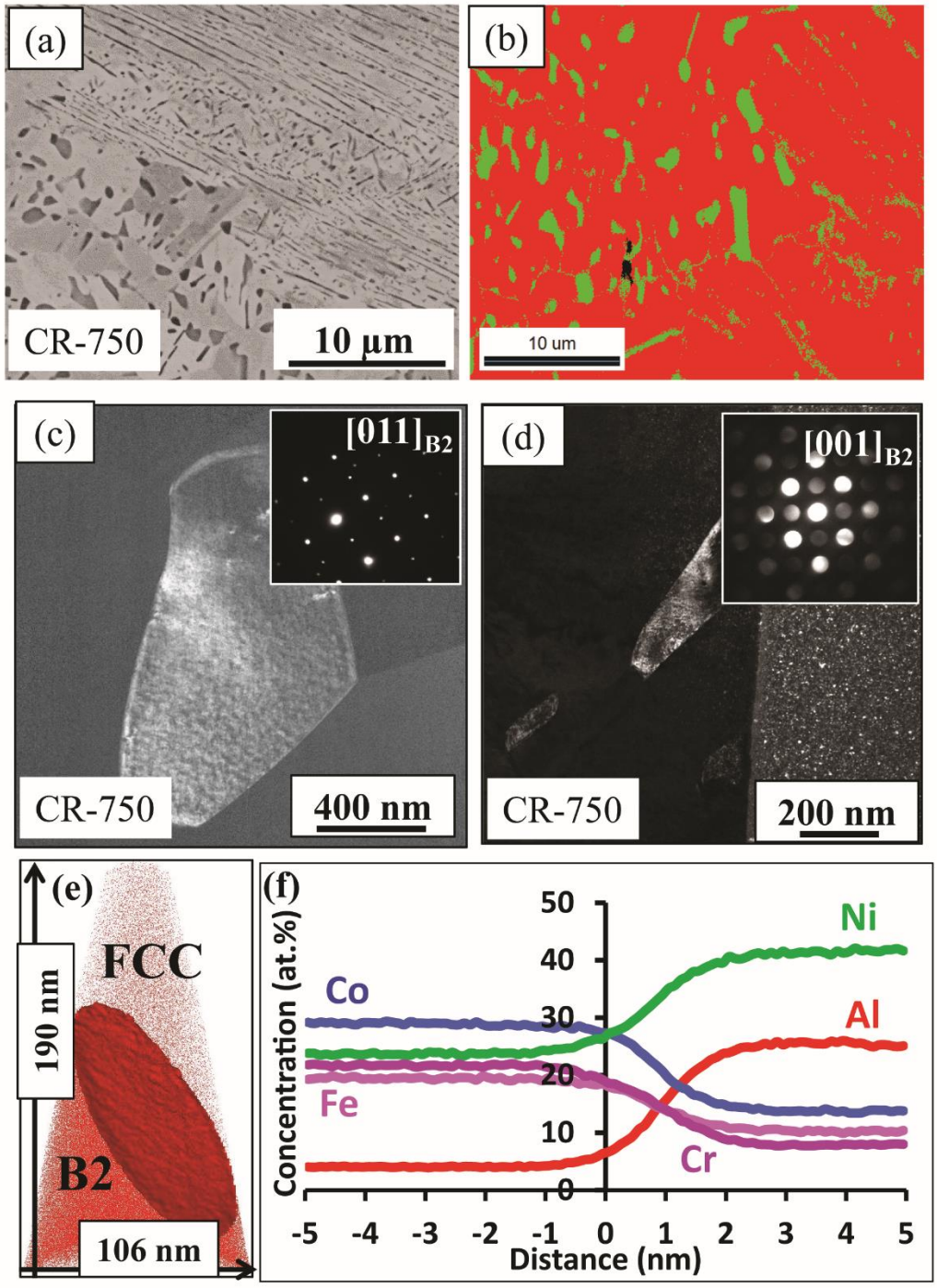

Figure 5: (a) BSE contrast SEM image from $Al_{0.5}Co_{1.5}FeNi_{1.5}$ in CR-750 condition (b) Higher magnification phase-map acquired using EBSD, from the same condition. (c) Dark-field TEM image acquired using superlattice spot from [011] zone axis of B2 phase in recrystallized region. (d) Dark-field TEM image acquired using superlattice spot from [011] zone axis of B2 plate along a twin in unrecrystallized region. (e) APT reconstruction showing an FCC/B2 interface, along with the corresponding proxigram depicting FCC/B2 compositions in (f). Figures reprinted from [24] with permission from Elsevier.

transformation including a displacive structural component along with solute diffusion. Plastic deformation results in formation of metastable intermediate structures in vicinity of twin interfaces, comprising of structural motifs which closely resemble BCC crystallographic symmetry necessary for K-S oriented B2 nucleation. Such structures are compositionally indistinguishable from the surrounding FCC matrix at the time of formation. Eventually, solute partitioning entails with annealing which drives the transformation of these pockets to B2 phase.

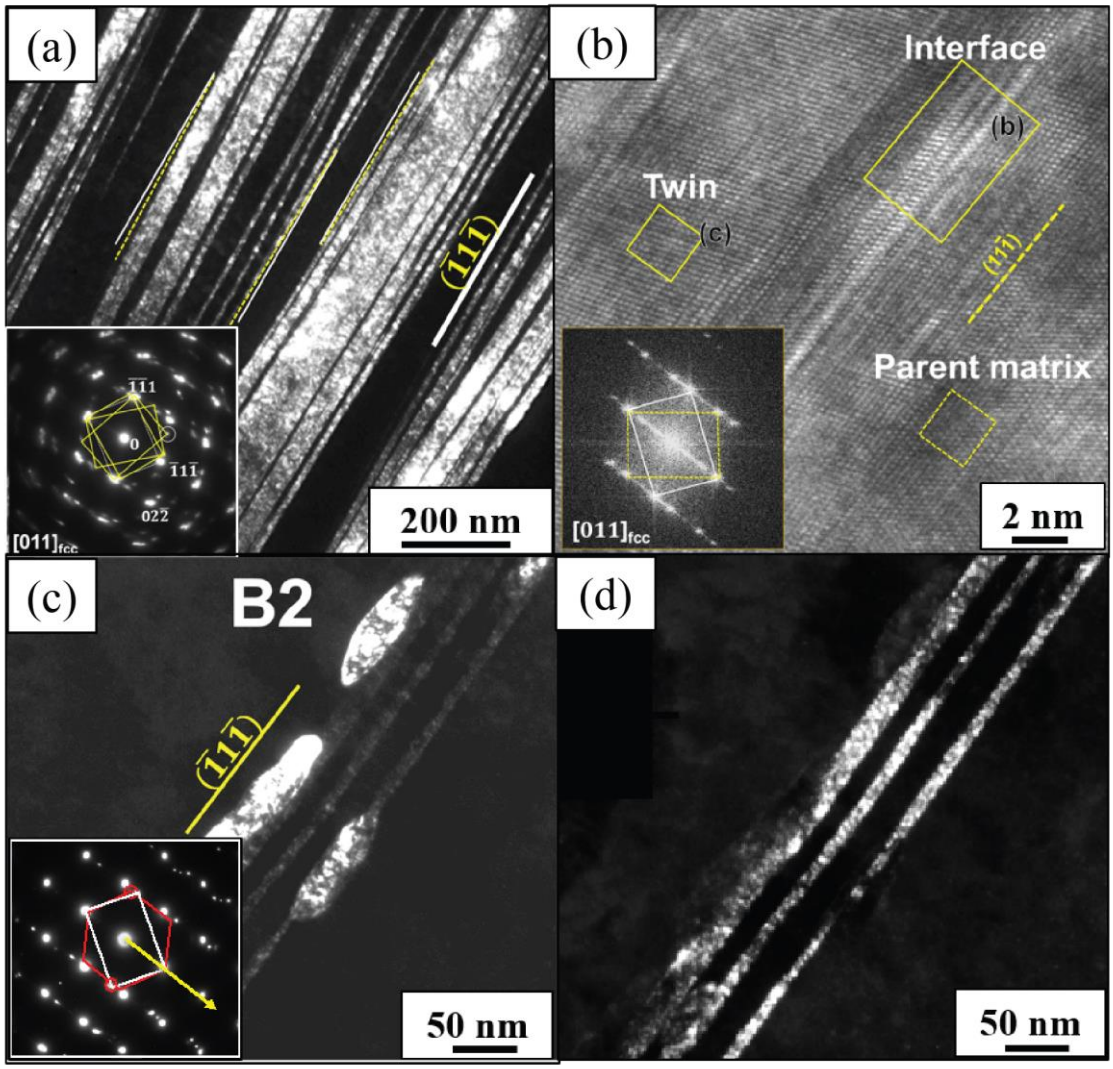

Figure 6: (a) Dark-field TEM image from cold-rolled sample showing high density of deformation twins oriented along (111) planes. (b) HRTEM image of a deformation twin along with corresponding FFT shown in inset. (c) Dark-field TEM image showing nucleation of B2 plates along twin boundaries after 30 minutes of annealing at 700°C. (d) Low magnification dark-field TEM image acquired using superlattice spot from B2 phase showing B2 plates decorating twin boundaries after annealing for 30 mins. Figures reprinted from [25] with permission from Elsevier.

In the present sample, the unrecrystallized region consists of coarse FCC grains without any $L1_2$, but fine-scale B2 precipitates aligned along deformation bands/twins which formed during cold-rolling. The composition of these B2 precipitates was examined via APT. Figure 5(e) is an APT reconstruction along with the corresponding proxigram shown in Figure 5(f). From the composition data, it appears that the B2 precipitates follow the stoichiometry: (Ni,Co)(Al,Co,Cr,Fe) assuming NiAl type stoichiometry [26,27]. Although B2 phase has a higher barrier to homogenous nucleation within an FCC matrix, the high density of defects structures such as grain boundaries, deformation bands, twins, and dislocation tangles, serve as potent sites for heterogenous nucleation of B2 phase, resulting in a microstructure with much higher volumefraction of B2 than that in previous case (i.e. CRSA750). This also indicates that the nucleation and growth of B2 phase results in depletion of the solute saturation from within the FCC matrix because the metastable $L1_2$ phase no longer precipitates out along with the B2, as was observed in the case of CRSA-750 condition. Hence, employing defect mediated nucleation of equilibrium phase may inhibit the formation of metastable phases which might be otherwise unavoidable via conventional processing route.

3) Competing nucleation tendencies between metastable $L1_2$ and multiple equilibrium phases in $Al_{0.3}CoCrFeNi$

In the foregoing section, it was established that the competition between nucleation of metastable and equilibrium phases can be influenced by introducing a large density of heterogenous nucleation sites in the microstructure via cold rolling. The present section explores the microstructural evolution when nucleation of multiple equilibrium phases compete with that of a metastable phase.

In this case, the homogenized $Al_{0.3}CoCrFeNi$ alloy was cold rolled to ~50% reduction in thickness which was then directly annealed at 700°C for 96 hrs [25]. The CALPHAD calculations shown in Figure 1(a) predict the equilibrium phase field to consist of (FCC+B2+σ). As explained above, the annealing temperature was selected to ensure a ternary phase-field in the present case. Samples were analyzed from intermediate stages of annealing as well, to understand the microstructural evolution with annealing time [25]. The microstructure in the cold rolled sample consists of high density of deformation twins. This is shown in the dark-field TEM image shown in Figure 6(a) and the HRTEM image in Figure 6(b). With as short as 30 minutes of aging, B2 plates start

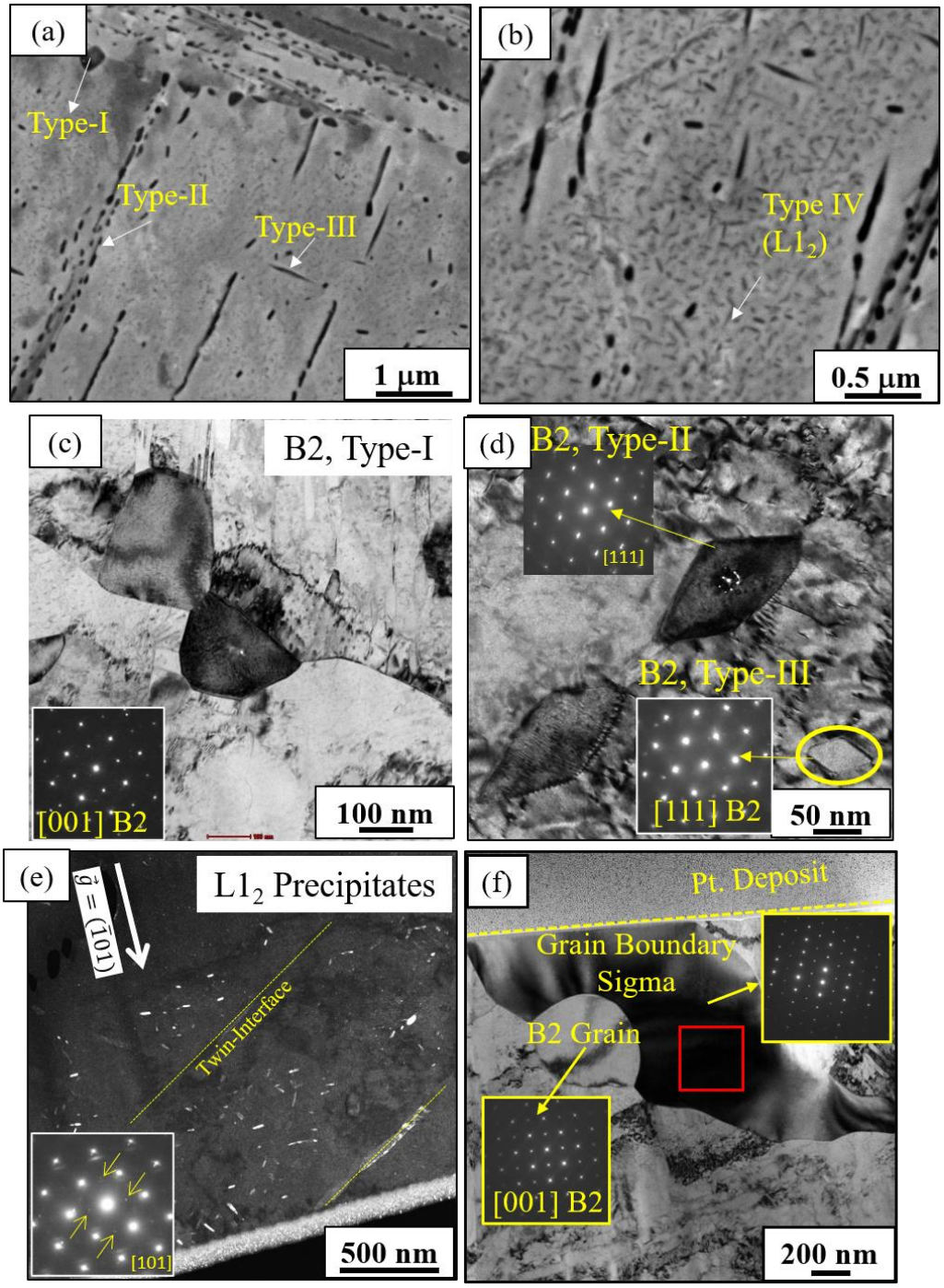

Figure 7: (a) Low magnification BSE contrast SEM image, and (b) High magnification BSE contrast SEM image, both from $Al_{0.3}$CoCrFeNi in CR-96 condition. (c) Bright-field TEM image showing presence of Type-I B2 along prior FCC grain boundary (d) Brigth-field image showing Type-III B2 precipitate along a twin boundary and a Type-III B2 precipitate within the FCC matrix. (e) Dark-field TEM image acquired using superlattice reflection showing presence of $L1_2$ precipitates. (f) Bright-field TEM image showing nucleation of grain-boundary sigma phase adjacent to a Type-I B2 grain. Figures reprinted from [25] with permission from Elsevier.

nucleating along these twins as shown in Figures 6(c) and (d), which are both dark-field TEM images. The density of such B2 plates increase eventually with aging time. With about 4 hours of annealing (CR-4 condition), nucleation of B2 along grain boundary starts. With increasing annealing time, EBSD indicates an increase in twin-boundary density owing to increase in number of annealing twins which then serve as additional nucleation sites for B2 phase. As a result, larger heterogenous nucleation sites are available for B2 precipitates to form leading to an increase in B2 density with aging time. After 96 hours of annealing (CR-96 condition), multiple generations and types of precipitates have nucleated along various defects in the microstructure as well as within the FCC matrix.

a. Type I: These are fine-scale recrystallized B2 grains nucleated along prior FCC grain-boundaries and triple-junctions. Figure 7(a) is a BSE contrast SEM image showing their presence along FCC grain boundaries. Further, a bright-field TEM image from such a precipitate is also shown in Figure 7(c).
b. Type II: These are elongated, pancake shaped B2 precipitates forming along twin boundaries within the FCC grains. They are marked in Figure 7(a) along with a representative bright-field TEM image showing their presence along twin boundaries in Figure 7(d).
c. Type III: These are faceted B2 precipitates nucleating within FCC grains in regions away from twin boundaries, probably either along dislocation tangles or nucleating homogeneously. These are also marked in Figure 7(a) along with an example shown in Figure 7(d).
d. Type IV: These are fine-scale metastable $L1_2$ precipitates in regions within adjacent twin bands decorated with Type-II B2 precipitates. These are marked in Figure 7(b) which is a BSE-contrast SEM image. Their presence was also confirmed by dark-field TEM imaging acquired using the superlattice reflection, as shown in Figure 7(e).
e. σ grains nucleate adjacent to Type-I B2 grains along prior-FCC grain-boundaries as shown by the bright-field TEM image in Figure 7(f).
f. Cr-rich BCC pockets adjacent to Type-II B2 precipitates along twin interfaces. An example is shown in Supplementary Figure S2(a) which is an STEM-EDS map of

Cr showing Cr rich pocket along a twin boundary, along with micro-diffraction pattern shown in inset of Supplementary Figure S2(b) which is a DF-TEM image.

Figure 8 shows that the homogeneous nucleation of B2 directly within the FCC matrix at 700°C is associated with a higher onset-driving force, but again due to a high nucleation barrier, it is instead nucleating heterogeneously along various high energy defects such as triple-junctions, grain boundaries, twin-interfaces, and dislocation tangles. Also, Type-II and Type-III B2 precipitates both maintain K-S orientation relationship with the parent FCC matrix.

As discussed previously, although $L1_2$ phase is not an equilibrium phase at this temperature as predicted by CALPHAD (see Figures 1(a) and (d)), it forms in the current system owing to a finite driving force (see Figure 8) [7] coupled with a low nucleation barrier to homogenous nucleation within the FCC matrix. Such $L1_2$ precipitates only exist in regions farther away from twin bands decorated with B2 phase because the nucleation and growth of B2 phase, renders the regions surrounding twin bands, poorer in Ni and Al hence, making nucleation of $L1_2$ compositionally challenging.

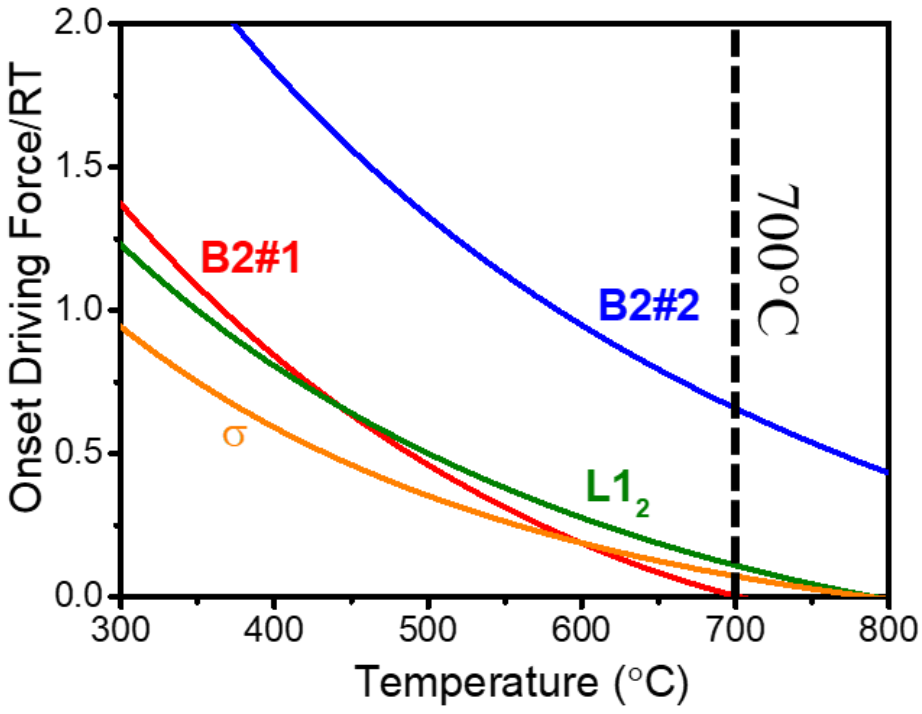

Figure 8: Normalized onset-driving forces for homogeneous nucleation within an FCC matrix for various phases in alloy $Al_{0.3}CoCrFeNi$, determined using ThermoCalc, as a function of temperature. Figure reprinted from [25] with permission from Elsevier.

Nucleation and subsequent growth of Ni and Al rich Type-I B2 grains at prior FCC grain-boundaries leads to Cr enrichment adjacent to these B2 precipitates which is conducive for heterogenous nucleation of σ phase here which is otherwise difficult. Just like in the case of B2 phase, the difficulty in homogenously nucleating sigma arises out of a prohibitively high energy barrier to nucleation within an FCC matrix despite having a finite onset-driving force, which can be seen from Figure 8. Formation of Ni and Al rich Type-II B2 precipitates also result in pockets of Cr enrichment along twin boundaries with BCC structure which may be precursors to σ phase. Being embedded within the FCC matrix perhaps prevents their transformation owing to a high barrier for nucleation of σ phase within an FCC matrix which is not the case with those pockets which are situated along grain boundaries. Therefore, multiple occurrences of sigma grains along prior grain boundaries have been observed in the present condition whereas no instances of sigma phase within an FCC grain was observed.

Conclusion

In the present study, defects induced during processing of HEAs/CCAs are used to promote heterogenous nucleation of equilibrium B2 phase along high energy defects such as grain boundaries, deformation twins, annealing twins, deformation bands, dislocation tangles, etc. Conventional processing route of solutionizing after cold rolling followed by annealing, may not always result in the equilibrium phases in their predicted volume fractions, for these alloys. While this is true for all the three alloys reported in this study, sometimes a metastable $L1_2$ phase may nucleate homogeneously in competition with the equilibrium phase (the case of $Al_{0.5}Co_{1.5}CrFeNi_{1.5}$ alloy). This stems from a high nucleation barrier for the equilibrium phases in FCC matrix while a much lower barrier to nucleation of the metastable $L1_2$ phase exists. A large density of defect induced heterogenous nucleation sites bias this competition in the favor of the equilibrium B2 phase (the case of $Al_{0.5}Co_{1.5}CrFeNi_{1.5}$). The scenario is further complicated when more than one equilibrium phase competes for nucleation with the metastable $L1_2$ phase with a lower nucleation barrier which was the case for $Al_{0.3}CoCrFeNi$ alloy. Whereas annealing this alloy in cold rolled condition within a ternary phase field results in nucleation of multiple generations of B2 precipitates along twin boundaries, within the FCC grains, and along prior FCC grain boundaries with σ grains, system favors the nucleation of $L1_2$ precipitates over B2 in the FCC matrix, again owing to a lower nucleation barrier of $L1_2$ as compared to B2. In all three alloys, such

heterogeneously templated microstructure results from a prior step of introducing high defect density via processing, before annealing conventionally. Previously published literature has highlighted achievement of an attractive balance in mechanical properties from such a microstructure, when compared to the conventionally processed counterparts [6,24,25]. This has been possible due to the existence of multiphase equilibrium domains within the complex phase diagrams associated with HEAs/CCAs. In summary, such an approach can be exploited to tailor the microstructure in case of other HEAs as well to gain a handle over their mechanical properties.

Acknowledgments:

The work was supported by the US Air Force Office of Scientific Research under grant FA9550-17-1-0395. The authors acknowledge the Materials Research Facility (MRF) at the University of North Texas for use of microscopy and characterization facilities. BG would like to acknowledge the support by Pacific Northwest National Laboratory's (PNNL) open call laboratory directed research and development (LDRD) program. PNNL is a multi-program national laboratory operated by Battelle for the U.S. DOE under Contract DE-AC05-76RL01830.

Declaration of Competing Interest:

The authors declare that they have no conflicting interests which may influence the results reported in this paper.

References:

1. P. Sathiyamoorthi and H. Seop Kim, Progress in Materials Science 100709 (2020).
2. R. S. Mishra, R. S. Haridas, and P. Agrawal, Materials Science and Engineering: A 141085 (2021).
3. Y. Zhu, K. Ameyama, P. M. Anderson, I. J. Beyerlein, H. Gao, H. S. Kim, E. Lavernia, S. Mathaudhu, H. Mughrabi, R. O. Ritchie, N. Tsuji, X. Zhang, and X. Wu, Materials Research Letters **9**, 1 (2021).
4. D. B. Miracle and O. N. Senkov, Acta Materialia **122**, 448 (2017).
5. B. Cantor, Progress in Materials Science 100754 (2020).
6. S. Dasari, B. Gwalani, A. Jagetia, V. Soni, S. Gorsse, and R. Banerjee, Scientific Reports **10**, 1 (2020).
7. B. Gwalani, S. Gorsse, D. Choudhuri, M. Styles, Y. Zheng, R. S. Mishra, and R. Banerjee, Acta Materialia **153**, 169 (2018).
8. S. Dasari, Y.-J. Chang, A. Jagetia, V. Soni, A. Sharma, B. Gwalani, S. Gorsse, A.-C. Yeh, and R. Banerjee, Materials Science and Engineering: A **805**, 140551 (2021).
9. B. Gwalani, S. Gorsse, D. Choudhuri, Y. Zheng, R. S. Mishra, and R. Banerjee, Scripta Materialia **162**, 18 (2019).

10. B. Gwalani, A. V. Ayyagari, D. Choudhuri, T. Scharf, S. Mukherjee, M. Gibson, and R. Banerjee, Materials Chemistry and Physics **210**, 197 (2018).
11. M.-H. Tsai, K.-Y. Tsai, C.-W. Tsai, C. Lee, C.-C. Juan, and J.-W. Yeh, Materials Research Letters **1**, 207 (2013).
12. R. Feng, M. C. Gao, C. Zhang, W. Guo, J. D. Poplawsky, F. Zhang, J. A. Hawk, J. C. Neuefeind, Y. Ren, and P. K. Liaw, Acta Materialia **146**, 280 (2018).
13. S. Dasari, A. Jagetia, V. Soni, B. Gwalani, S. Gorsse, and R. Banerjee, Materials Research Letters **8**, 399 (2020).
14. Z. Wu, H. Bei, G. M. Pharr, and E. P. George, Acta Materialia **81**, 428 (2014).
15. A. Jagetia, M. S. K. K. Y. Nartu, S. Dasari, A. Sharma, B. Gwalani, and R. Banerjee, Materials Research Letters **9**, 213 (2021).
16. B. Gwalani, V. Soni, M. Lee, S. Mantri, Y. Ren, and R. Banerjee, Materials & Design **121**, 254 (2017).
17. H. R. Sistla, Joseph. W. Newkirk, and F. Frank Liou, Materials & Design **81**, 113 (2015).
18. S. Niu, H. Kou, T. Guo, Y. Zhang, J. Wang, and J. Li, Materials Science and Engineering: A **671**, 82 (2016).
19. C. Li, J. C. Li, M. Zhao, and Q. Jiang, Journal of Alloys and Compounds **504**, S515 (2010).
20. J. Y. He, H. Wang, Y. Wu, X. J. Liu, H. H. Mao, T. G. Nieh, and Z. P. Lu, Intermetallics **79**, 41 (2016).
21. Y. L. Zhao, T. Yang, Y. Tong, J. Wang, J. H. Luan, Z. B. Jiao, D. Chen, Y. Yang, A. Hu, C. T. Liu, and J.-J. Kai, Acta Materialia **138**, 72 (2017).
22. J. Y. He, H. Wang, H. L. Huang, X. D. Xu, M. W. Chen, Y. Wu, X. J. Liu, T. G. Nieh, K. An, and Z. P. Lu, Acta Materialia **102**, 187 (2016).
23. Y.-J. Chang and A.-C. Yeh, Journal of Alloys and Compounds **653**, 379 (2015).
24. S. Dasari, A. Jagetia, Y.-J. Chang, V. Soni, B. Gwalani, S. Gorsse, A.-C. Yeh, and R. Banerjee, Journal of Alloys and Compounds **830**, 154707 (2020).
25. S. Dasari, A. Sarkar, A. Sharma, B. Gwalani, D. Choudhuri, V. Soni, S. Manda, I. Samajdar, and R. Banerjee, Acta Materialia **202**, 448 (2021).
26. N. V. Allaverdova, V. K. Portnoy, L. A. Kucherenko, A. V. Ruban, and V. I. Bogdanov, Journal of the Less Common Metals **139**, 273 (1988).
27. Y. L. Hao, R. Yang, Y. Song, Y. Y. Cui, D. Li, and M. Niinomi, Materials Science and Engineering: A **365**, 85 (2004).
28. D. Choudhuri, S. Shukla, W. B. Green, B. Gwalani, V. Ageh, R. Banerjee, and R. S. Mishra, Materials Research Letters **6**, 171 (2018).
29. D. Choudhuri, S. Shukla, B. Gwalani, R. Banerjee, and R. S. Mishra, Materials Research Letters **7**, 40 (2019).